VHCF ultrasonic tests on EN AW6082 aluminum alloy samples over a wide dimensional range

Original
VHCF ultrasonic tests on EN AW6082 aluminum alloy samples over a wide dimensional range / Montagnoli, F., Invernizzi, S., Carpinteri, A.. - In: FATIGUE & FRACTURE OF ENGINEERING MATERIALS & STRUCTURES. - ISSN 8756-758X. - STAMPA. - 46:8(2023), pp. 3099-3117. [10.1111/ffe.14056]

Publisher:
Wiley

Published
DOI:10.1111/ffe.14056

Received: 20 December 2022 | Revised: 25 April 2023 | Accepted: 3 May 2023
DOI: 10.1111/ffe.14056

SPECIAL ISSUE ARTICLE

FFEMS Fatigue & Fracture of Engineering Materials & Structures

WILEY

VHCF ultrasonic tests on EN AW-6082 aluminum alloy samples over a wide dimensional range

Francesco Montagnoli[1] | **Stefano Invernizzi**[1] | **Alberto Carpinteri**[1,2]

[1]Department of Structural, Geotechnical and Building Engineering, Politecnico di Torino, Turin, Italy

[2]Department of Civil and Environmental Engineering, Shantou University, Shantou, China

Correspondence
Stefano Invernizzi, Politecnico di Torino, Corso Duca degli Abruzzi 24, Turin, Italy.
Email: stefano.invernizzi@polito.it

Abstract

In the present paper, a very high cycle fatigue test campaign carried out with an ultrasonic testing machine up to 10^{10} cycles is presented. The aluminum alloy hourglass and dog-bone samples have dimensions spanning over a very wide range, with the diameter in the middle cross-section comprised between 3 and 30 mm. From the experimental results, the influence of structural size can be clearly detected, and it is possible to observe a transition between small scales, where the size effect is more pronounced, and larger scales, where the size effect is vanishing. This phenomenon can be explained in an effective way by adopting a multifractal formalism, which is equipped with the probabilistic treatment of the statistical dispersion of experimental data.

KEYWORDS

multifractality, probabilistic specimen size-dependent S-N curves, very high cycle fatigue, wide size range

Highlights

- Ultrasonic very high cycle fatigue tests are performed on EN AW-6082 samples.
- The size and the critical volume of samples span over one and two orders of magnitude.
- The size effect is clearly observed and interpreted thanks to the multifractal formalism.
- The multifractal scaling law is equipped with a probabilistic treatment of the results.

Abbreviations: A-D, Anderson-Darling; ASTM, American Society for Testing and Materials; CDF, cumulative distribution function; CvM, Cramer-von Mises; K-S, Kolmogorov-Smirnov; MFSL, multifractal scaling law; MLM, maximum likelihood method; P, probability; P-S-N, probabilistic stress-life; *P*-S-N-*b*, specimen size-dependent probabilistic stress-life; SEM, scanning electron microscope; UFTM, ultrasonic fatigue testing machine; VHCF, very high cycle fatigue.

1 | INTRODUCTION

During the last few decades, the growing need to extend the design fatigue lifetime of mechanical structural components led to increasing interest in the understanding of the fatigue behavior in the very high cycle fatigue regime of metallic materials.[1] An important support in the comprehension of VHCF behavior of metallic materials is due to the introduction of ultrasonic fatigue testing machines, which have allowed to reduce the testing time. The first attempt to increase the working frequency of fatigue testing machines can be traced back to the '50s, when Mason discovered that ultrasounds generated by piezoelectric transducers are able to induce fatigue fractures in the materials.[2–4] Since then, many steps forwards have been made in the understating of the crack initiation mechanisms of metallic materials in the gigacycle regime. More recently, it has also been demonstrated that the very high cycle fatigue phenomenon should be also considered in the assessment of the fatigue lifetime of existing structures and infrastructures that were built during the last century. In fact, the authors of the present contribution have demonstrated as the very high cycle low-amplitude fatigue may have been one of the possible causes to explain the collapse of the Morandi bridge (Italy).[5–8]

Another crucial research field in the gigacycle fatigue domain is the study of the specimen size effect that afflicts the VHCF strength.[9–11] In fact, it is well known in the literature the importance of the specimen size influence on the static tensile strength. To this aim, an important step forward in the comprehension of size effect on the nominal tensile strength of concrete structures was given by Alberto Carpinteri in the '90s, who exploited the concepts of fractal geometry to give a theoretical explanation to this phenomenon.[12,13] Analogously, size-effects on the high-cycle fatigue resistance of metallic materials have been also extensively investigated over the past decades.[14–17] Unfortunately, since the VHCF is an enough young research field, size effects on the gigacycle fatigue are not yet deeply investigated. In fact, only during the last decade, a lot of theoretical and experimental studies have been performed to analyze the influence of specimen size on the VHCF resistance. Thanks to this first investigations, it was possible to understand the right importance of this research field in the prediction and comprehension of the VHCF response of metallic materials.[18] More in detail, different experimental campaigns have demonstrated a decrement in the gigacycle fatigue resistance by increasing the specimen size.[19] Nowadays, it is well known that inherent defects within the risk-volume are often potential crack initiation sites. In other words, the VHCF response of a material is governed by the defect population embedded in the volume.[20] According to Murakami's model,[21] the VHCF resistance depends on the size of the largest inclusion within the risk-volume.[22,23] Moreover, a lot of experimental campaigns have highlighted that the probability to find a larger defect size increases with the risk-volume.[24] In other words, the larger the risk-volume, the higher the probability to find larger defects, and consequently the lower the fatigue resistance experienced by the structural component.[25,26] Unfortunately, it is unfeasible to test full-scale components by adopting an ultrasonic fatigue testing machine. In fact, gigacycle fatigue tests are commonly carried out on very small specimens with standard dimensions.[27] Conversely, very large components could be easily tested with standard fatigue testing equipment. At the same time, it is extremely complex and time-consuming to investigate the VHCF domain, since a number of cycles higher than 10–100 million would require more than 1 month by adopting servo-hydraulic and rotating bending testing machines, working at cyclic frequencies below 100 Hz.[28] As a matter of fact, it follows that the VHCF resistance of full-scale components should be only extrapolated through theoretical models.[29] As a consequence, it is difficult to fully validate the available theoretical models for the prediction of the specimen size effect on the VHCF resistance, due to the lack of fatigue experimental data spanning over a wide dimensional range.

In the present paper, ultrasonic fatigue tests in the very high cycle fatigue (VHCF) range were conducted on a set of EN AW-6082 aluminum alloy hourglass and dogbone specimens spanning over a wide dimensional range. The diameter of the ligament of each sample set was respectively: 3, 6, 12, 24, and 30 mm. The sample shape of each set was such that the first free vibration frequency was equal to 20 kHz and that the stress concentration factor in the ligament cross-section did not exceed 1.1. Therefore, the risk volume of the largest specimen was almost 300 times that of the smallest one, based on finite element calculation. The obtained experimental results showed a clear and pronounced scale effects for the smaller specimens, whereas for larger scales a much less significant decrement in the fatigue resistance was found. Subsequently, the multifractal formalism was adopted to explain the observed specimen size effect in the VHCF regime of the EN AW-6082 aluminum alloy. The multifractal formalism was combined with classical statistical concepts, adopting a two-parameter Weibull distribution, in order to account for the statistical dispersion of the experimental results. In this way, it was possible to derive the analytical relationship for the probabilistic scale-dependent P-S-N-b curves, which makes it possible to predict the VHCF life as a function of the structural component size and the probability of survival. Eventually, the fatigue experimental results, obtained by the authors, were exploited to fit the experimental results and to check the accuracy and the reliability of the model in the prediction of the VHCF life with different failure probability under constant-amplitude fatigue loadings.

2 | EXPERIMENTAL METHODOLOGY

2.1 | Material

Hourglass and dog-bone specimens subjected to ultrasonic VHCF tests were made of EN AW-6082/AlSi1MgMn (according to the designation given in EN 573:3 2019[30]), which were subjected to a solutionizing-artificial aging (T6) heat treatment. EN AW-6082 is one of the most popular alloys of the 6xxx aluminum-magnesium-silicon family. In addition, since the investigated EN AW-6082 is characterized by good tensile strength and excellent corrosion resistance, it is often used in structural components subjected to low-amplitude fatigue loads at a very high number of cycles (offshore constructions, machine buildings, and mobile cranes).

The virgin material was provided in three cylindrical rods of 20, 30, and 40 mm in diameter and 4 m in length, which were obtained from the same batch. An automating CNC machining process was exploited to shape the specimens used for the experimental tests. Moreover, the physical and mechanical properties of EN AW-6082 used for the ultrasonic fatigue tests were assessed. The mass density, ρ, was determined by using an analytical weight balance Kern® ALJ 310-4A, which is characterized by a resolution of ±0.1 mg and linearity of ±0.3 mg. The longitudinal dynamic elastic modulus, E_d, was obtained according to ASTM Standard E1876-15.[31] First, one cylindrical sample of 6 mm in diameter and 120 mm in length was obtained through a machining process from each of the original cylindrical rods. After that, the non-destructive impulse excitation technique was exploited to measure the first longitudinal resonance frequency of each cylindrical sample, so that it was possible to assess the corresponding longitudinal dynamic elastic modulus. The procedure was repeated six times for each cylindrical sample. Hence, the average value of the dynamic Young's modulus for the three cylindrical rods was assessed by adopting the formula reported in ASTM Standard E1876-15,[31] whereas the corresponding standard deviation was analytically determined by using the Law of Propagation of Uncertainty. In addition, Brinell hardness HB was measured for the three round bars according to ASTM Standard E10-18.[32] The average values of the physical and mechanical quantities are summarized in Table 1, together with the corresponding standard deviations. From this table, it can be stated that the standard deviations were always limited for all measured mechanical quantities.

TABLE 1 Physical and Brinell hardness of the investigated EN AW-6082 aluminum alloy.

Rod Φ (mm)	ρ (kg/m^3)	E_d (kg/m^3)	Brinell hardness (HB)
20	2713 ± 5.9	72.3 ± 0.1	105 ± 1.4
30	2700 ± 7.4	70.1 ± 0.2	102 ± 1.7
40	2700 ± 9.4	70.4 ± 0.2	100 ± 0.7

Finally, the ultimate tensile strength, σ_u, the yield stress, σ_y, and the ultimate deformation, ϵ_u, were determined on two dog-bone specimens for each cylindrical rod, which were subjected to tensile tests. The samples were shaped with different diameters to determine the size effect on the tensile static mechanical properties of the investigated material. More in detail, dog-bone specimens of 6 and 12 mm in diameter were, respectively, obtained by shaping the cylindrical rods of 20 and 30 mm in diameter according to ASTM Standard B557M-15.[33] At this stage, it could be specified that the dog-bone specimens of 6 mm in diameter were not obtained from the same batch of the other ones. The self-similar dog-bone specimens of 24 mm in diameter were obtained by shaping the rod of 40 mm in diameter.[33] In all the cases, the tensile tests were performed under displacement control by using a servo-hydraulic tensile test machine with a 500 kN load cell. In Figure 1, the engineering stress–strain curve for the sample of 12 mm in diameter is reported. In addition, the average values and the corresponding standard deviations of the static mechanical quantities are summarized in Table 2 as a function of the diameter in the middle cross-section, d, and the adopted gauge length, l_0. From this table, it is interesting to note that clearly emerges a negative dependence of the ultimate tensile strength on the specimen size, d, as well as a decrement in the ultimate strain is obtained as a function of the gauge length, l_0. These two trends are perfectly consistent with the explanation given in Carpinteri et al,[34] where the scaling of the ultimate tensile strength and the ultimate strain is described by power-laws with negative exponents.

2.2 | Ultrasonic fatigue specimen design

To investigate the specimen size effect on the fatigue resistance of aluminum alloy EN AW-6082, ultrasonic fatigue tests were carried out on three different sets of

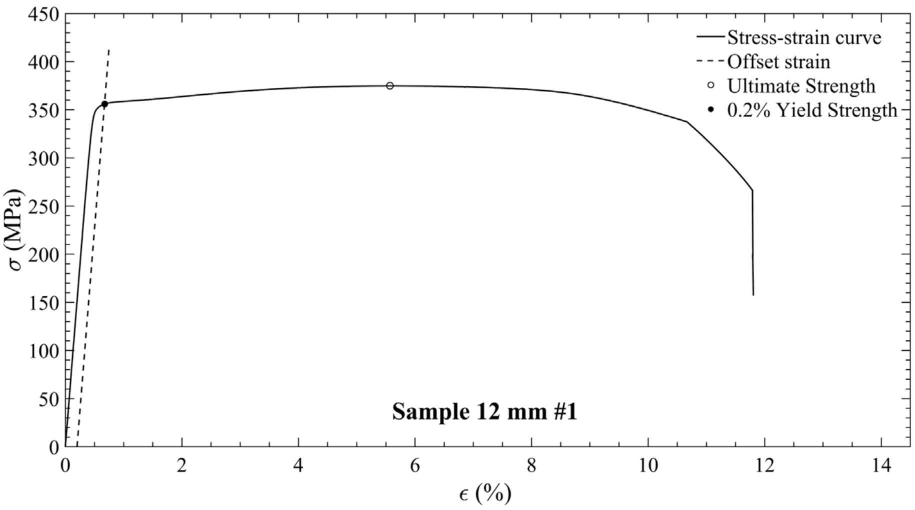

FIGURE 1 Engineering stress–strain curve for the sample of 12 mm in diameter.

TABLE 2 Static mechanical properties of the investigated EN AW-6082 aluminum alloy.

d (mm)	l_0 (mm)	σ_y (MPa)	σ_u (MPa)	ϵ_u (%)
6	35.2	389.2 ± 3.2	455.6 ± 2.2	18.4 ± 0.7
12	65	356.8 ± 1.3	375.1 ± 0.2	11.1 ± 1.0
24	65	308.1 ± 0.4	329.8 ± 0.1	14.5 ± 0.2

TABLE 3 Dynamic mechanical properties and risk volume of the investigated five different specimens.

Specimen	k_σ (MPa/µm)	f_{FEM} (Hz)	k_t (–)	V_{90} (mm^3)
3 mm	7.474	20,213	1.021	42
6 mm	4.233	20,047	1.025	301
12 mm	3.191	19,977	1.046	1731
24 mm	2.679	19,925	1.071	8928
30 mm	2.443	20,082	1.086	14,563

hourglass specimens, respectively, with diameters of 3, 6, and 12 mm in the middle cross-section. More in detail, the cylindrical rod of 20 mm in diameter was exploited to shape the specimens of 3 and 6 mm in diameter, whereas the specimens of 12 mm in diameter were obtained by the cylindrical rod of 30 mm. Furthermore, in order to enlarge the tested scale range, two sets of dog-bone specimens with diameters of 24 and 30 mm were also shaped by the largest cylindrical rod of 40 mm in diameter.

The preliminary geometry of hourglass and dog-bone specimens was obtained according to the equations reported in Bathias and Paris[35] and Liu et al,[36] respectively, as a function of the mass density and the dynamic longitudinal elastic modulus. In addition, the nominal normal stress k_σ in the middle cross-section of the specimen subjected to unit displacement amplitude was analytically assessed. Subsequently, the finite element analysis (FEA) software, ANSYS® Workbench, was exploited to verify the obtained geometry for all five different specimens. To this aim, a 2D reduced finite element model was created by using 8-node axisymmetric quadrilateral elements to discretise the specimen geometry. At first, a modal analysis was carried out to check that the fundamental longitudinal resonance frequency of the specimens is within the working frequency range of the ultrasonic fatigue testing machine. After that, the normal stress distribution within the specimen volume was checked by performing a harmonic analysis. To this aim, a nodal harmonic acceleration at the upper free end of the specimen was imposed. As a consequence, the stress concentration factor, k_t, evaluated according to Tridello et al,[37] and the risk volume, V_{90},[22,38,39] were obtained by the harmonic response analysis.

To this aim, it is worth noting that leading ultrasonic fatigue tests on large specimens is particularly challenging, since it is rather complicated to ensure the application of a sufficient stress amplitude able to fail the specimens with the maximum displacement amplitude provided by the UFTM. In fact, the value of the nominal normal stress in the middle cross-section substantially decreases with the specimen diameter. A possible way to increase the stress amplitude could be to enlarge both the diameters of the reduced central part and the extremity cylindrical one. On the other hand, a specimen can be considered "smooth" when the stress concentration factor is kept below 1.15. In other words, an increment in both the diameters of the specimen could be only adopted by increasing the length of the reduced central part in order to have about the same stress concentration factor, although this is not always possible. In fact, an increment in the length of the reduced central part implies a corresponding decrement in the length of the

FIGURE 2 The five different tested hourglass and dog-bone specimens. [Colour figure can be viewed at wileyonlinelibrary.com]

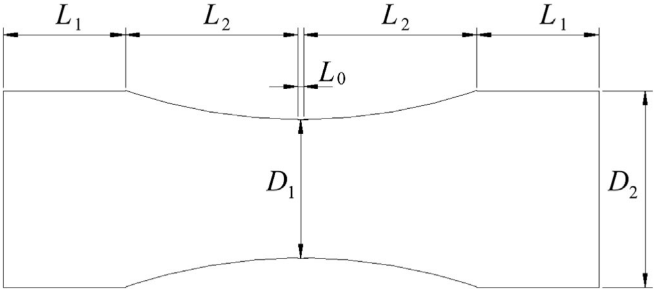

FIGURE 3 Ultrasonic specimen geometry.

TABLE 4 Dimensions of the five different specimens.

Specimen	D_1 (mm)	D_2 (mm)	L_1 (mm)	L_2 (mm)	L_0 (mm)
3 mm	3.0	10.0	10.1	20.0	0.0
6 mm	6.0	12.0	17.6	25.0	0.0
12 mm	12.0	20.0	17.1	30.0	0.0
24 mm	24.0	34.0	21.1	30.0	1.0
30 mm	30	39	24.0	30.0	1.0

FIGURE 4 Specimen of 12 mm in diameter equipped with T-rosette strain gauge. [Colour figure can be viewed at wileyonlinelibrary.com]

two cylindrical parts, since the first longitudinal natural frequency of the specimen has to be always close to 20 kHz. In other words, an optimization procedure was carried out to define the dimensions of the different parts of the specimen to ensure a high nominal stress amplitude, a small stress concentration factor, and a longitudinal resonance frequency of 20 kHz.

Thereafter, the preliminary geometry was iteratively modified to obtain a stress concentration factor smaller than 1.10 and a nominal normal stress k_σ for a unit displacement amplitude larger than 2.4, ensuring the first longitudinal natural frequency close to 20 kHz. In this iterative procedure, the specimen diameter in the middle cross-section was kept constant only, whereas all the other dimensions were modified to satisfy the target values in terms of stress concentration factor and nominal stress amplitude.

Table 3 shows the values of the nominal stress amplitude for a unit displacement amplitude, the stress concentration factor, the first longitudinal natural frequency, and the risk-volume for the five different specimens, whereas a photograph of the tested hourglass and dog-bone specimens is reported in Figure 2. In addition, the ultrasonic specimen geometry in a parametric form is reported in Figure 3, whereas Table 4 shows the actual dimensions of the five different specimens.

Moreover, it is relevant to observe that the largest specimen investigated in the present experimental campaign has dimensions much larger than the samples commonly used for ultrasonic fatigue testing in terms of both risk-volume and diameter in the middle cross-section.

Once obtained the desired geometry from numerical simulations, the hourglass and dog-bone specimens were obtained by means of a machining process. After that, all the specimens were mechanically polished with sandpapers to remove surface material defects due to the machining process and to obtain a final specimen surface roughness of 0.4 μm.

2.3 | Testing setup

VHCF tests were conducted under fully reversed constant stress amplitude tension-compression conditions ($R = -1$) at room temperature. Before to perform the experimental tests, the stress distribution was checked within the specimens of 6, 12, 24, and 30 mm in diameter by means of strain gauge measurements. T-rosette strain gauges in the half-bridge configuration were used to have the temperature compensation during the calibration procedure. The gauge signal was acquired at a minimum sampling rate of 300 kHz. Figure 4 shows the specimen of 12 mm in diameter equipped with the strain gauge rosette.

After the strain gauge calibration, the specimens were tested up to failure or up to a runout, which was fixed at 10^{10} cycles. To this aim, it was exploited the ultrasonic fatigue testing machine developed by the Italian company Italsigma® (UFTM MU90). The UFTM MU90 is composed by an ultrasonic generator (Branson® DCX Series S 4 kW), which generates an electric signal with a frequency of 20 kHz. The electric signal is converted into a sinusoidal mechanical vibration by the piezoelectric transducer (Branson® CR-20). A booster (Branson® 2000X Series Gold), rigidly connected to the piezoelectric converter through a screw connection, provides fixed support to the whole mechanical system and amplifies the displacement amplitude. The mechanical vibration is furtherly increased by the catenoidal horn (Branson® 126-192), which is assembled in line with the booster. Finally, the resonant system is composed of the specimen, connected through a screw connection to the horn and which can be subjected to a variable mechanical vibration spanning between 16 and 60 μm. The maximum value allowed for the displacement amplitude at the free end of the specimen was assessed to prevent unwanted failures of the horn. Furthermore, the mechanical vibration amplitude at the specimen bottom free end is monitored through an eddy current sensor (Micro-Epsilon® eddyNCDT 3300/3301). The acquired signal is used in a closed-loop circuit to keep the stress amplitude in the middle section of the specimen constant during the test. In other words, the nominal displacement amplitude is compared with the measured one and the power of the ultrasonic generator is adjusted accordingly in order to have a perfect match between them.

Furthermore, since the piezoelectric transducer works in the 19.5–20.5 kHz range, the axial fundamental frequency of all the components of the resonant system must be included within the same interval. On the other hand, the fatigue crack propagation toward the inner part of the specimen leads to an increase in the sample compliance and, as a consequence, a decrement in the resonance frequency will be expected. Therefore, if the fatigue crack propagates inside of the specimen up to a critical amount, its fundamental frequency will fall down the lower limit of 19.5 kHz. Consequently, the test will be automatically interrupted, since the piezoelectric transducer is no longer able to excite the whole resonant mechanical system.

During the VHCF tests, the specimen temperature was monitored with an infrared sensor (Optris® CT LT22CF). At the same time, an air-cooling system was used to control the temperature increment in the sample, which could occur due to internal heat arising from high-speed deformations in ultrasonic fatigue tests. It is worth noting that, before to perform the tests, the specimen surface was covered with a matte-black painting to increase its infrared emissivity (see Figure 5).

An additional way exploited in this experimental campaign to avoid unwanted heating of the specimens was to conduct intermittent VHCF tests. In this context, ultrasonic fatigue tests were continuously run for the hourglass specimens of 3 and 6 mm, since the sample temperature was kept close to the environment one by using the air-cooling system only. Vice versa, for the specimens of 12, 24, and 30 mm in diameter, the UFTM MU90 discontinuously operated in a pulse-pause mode. The pulse and pause lengths were set up at 500 and 500 ms, respectively. In this way, the temperature of the specimens of 12, 24, and 30 mm in diameter was kept below a pre-assigned value of about 50° C for almost the duration of tests, except for the final stage of the total fatigue life, when the specimen temperature rose abruptly just before failure due to the crack propagation.[40,41] It is reasonable to suppose that the higher self-heating of the specimens of 12, 24, and 30 mm is due to the larger sample dimensions, despite the investigated

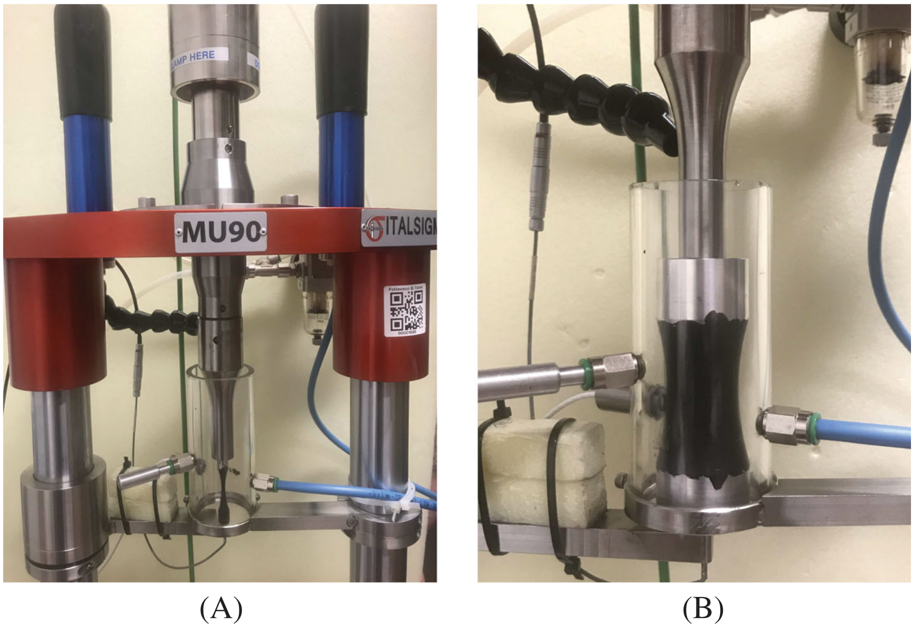
(A) (B)

FIGURE 5 Ultrasonic fatigue machine MU90 with the hourglass specimen of 3 mm (A) and the dog-bone specimen of 30 mm in diameter (B), both covered with a matte-black painting. [Colour figure can be viewed at wileyonlinelibrary.com]

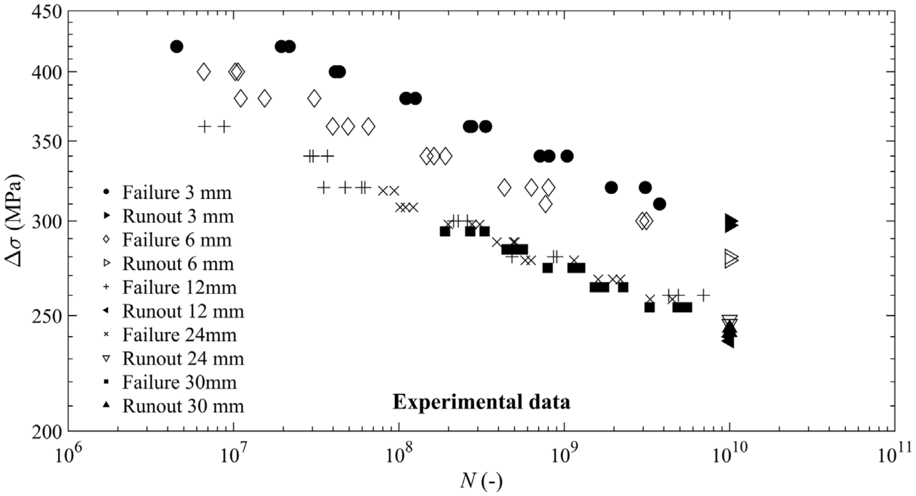

FIGURE 6 S-N diagram of the experimental data.

aluminum alloy is characterized by high thermal conductivity.

3 | EXPERIMENTAL RESULTS

Fatigue experimental data of EN AW-6082 T6 are shown in Figure 6, which were obtained under constant-amplitude loading conditions with a zero value of the mean stress ($R = -1$). For all the five different sets of specimens, failures were obtained in the range between 5×10^6 and 6×10^9 cycles, that is, in the VHCF regime. Twenty tests were carried out on hourglass specimens of 3 mm in diameter subjected to a stress range between a minimum value of 300 MPa and a maximum value of 420 MPa; 18 of these were tested up to failure, whereas two were runouts. Twenty tests were also carried out on specimens of 6 mm in diameter, reporting two runouts at a stress range of 280 MPa. Eighteen failures were obtained for the specimens of 12 mm in diameter between 260 and 360 MPa, whereas two runouts were obtained at a stress range value of 240 MPa. Twenty-one tests were carried out on specimens of 24 mm in diameter; 19 of these were tested up to failure, whereas two were runouts at a stress range of 248 MPa. Finally, 15 failures were obtained for the specimens of 30 mm in diameter between 254 and 294 MPa, whereas two runouts were obtained at a stress range of 244 MPa.

Fractographic analyses of broken specimens subjected to VHCF showed that the crack initiation site was always located at the sample surface. This experimental evidence is in perfect agreement with other experimental investigations regarding aluminum alloys received in overaged conditions.[42,43] Figure 7 shows the fracture surface

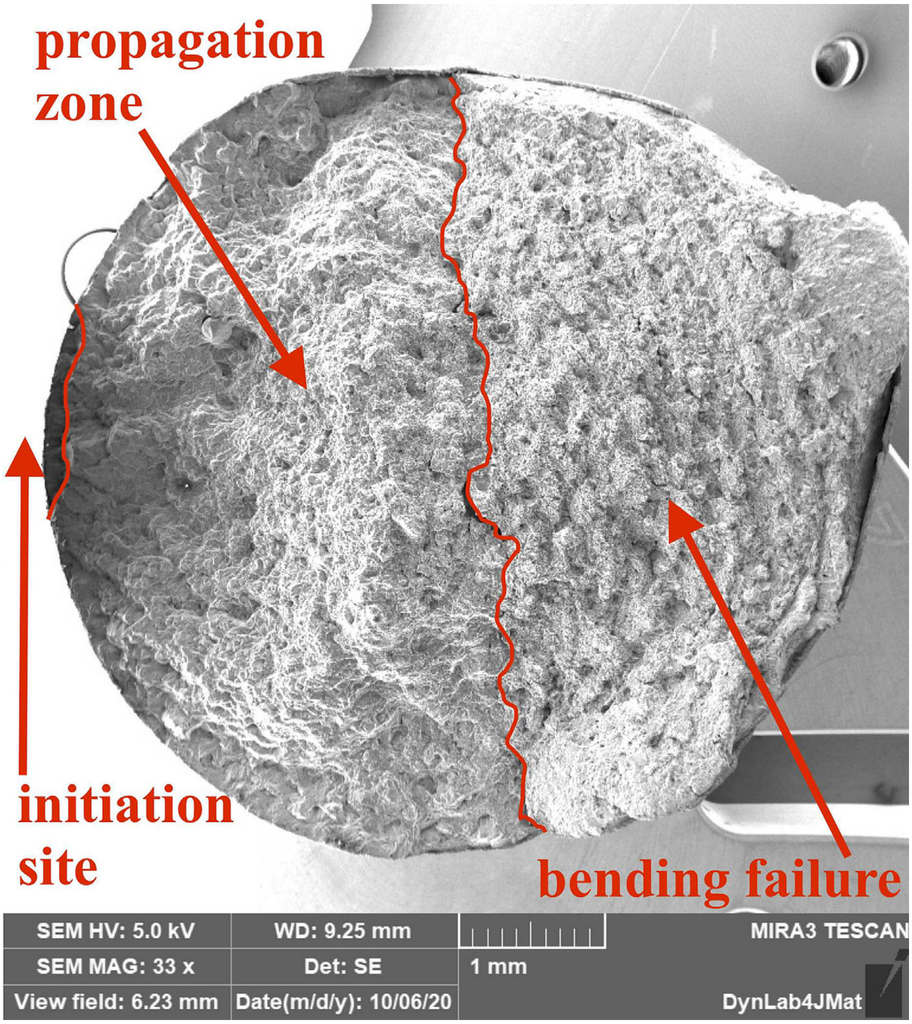

FIGURE 7 SEM image of the fracture surface morphology of the specimen of 6 mm in diameter that survived 49.258685×10^6 cycles at a stress range of 360 MPa. [Colour figure can be viewed at wileyonlinelibrary.com]

morphology of a specimen of 6 mm in diameter, which was subjected to a stress range of 360 MPa up to 49.258685×10^6 cycles. The fracture surface morphology was obtained by using a scanning electron microscope. From the figure, it is possible to clearly distinguish by naked eye the crack initiation site, the crack propagation zone, and the final failure region. It is worth noting that the total rupture of the specimen in two distinct parts was obtained with a 3-point bending test. In fact, the crack propagation during the ultrasonic test was such that the specimen frequency fell below the lower limit of 19.5 kHz, without yet leading to unstable and brittle crack propagation. A magnification of the crack initiation site (134×) shows that the crack path is oriented in a plane inclined to 45° with respect to the stress axis (see Figure 8), which is coherent with the experimental evidence observed in Höppel et al.[44]

A similar fracture surface morphology was obtained for the other specimen sizes. More in detail, in Figure 9, the fracture surface morphology for the specimen of 12 mm in diameter, which survived 259.331049×10^6 cycles at a stress range of 300 MPa, is reported. In this case, the fracture surface morphology was obtained by using an optical microscope. This figure shows characteristics of the fracture surface morphology very similar to that observed for the specimen of 6 mm in diameter. In particular, it is evident as the fatigue crack nucleation occurred at the sample surface, with the following crack propagation running at 45° to the stress axis.

A magnification of the crack initiation site (200×) showed that oxide coverings and abrasion were found ahead of the crack initiation site (see Figure 10), which were originated because of the fretting corrosion during the first crack advancements, as stated in Schwerdt et al.[43]

4 | *P*-S-N-*b* CURVES: SPECIMEN SIZE-DEPENDENT PROBABILITY-STRESS-LIFE CURVES IN THE SUPER-LONG-LIFE REGIME

In this section, the influence of specimen size on the probabilistic S-N curves in the VHCF range is

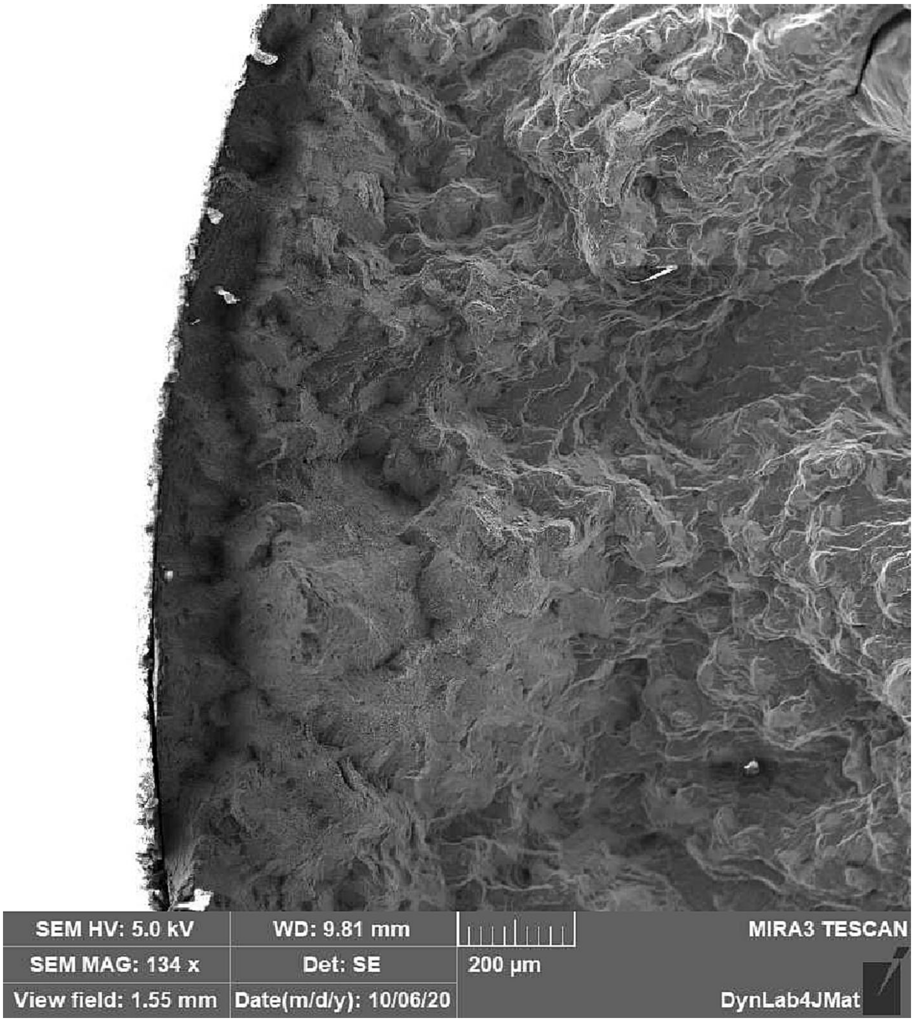

FIGURE 8 Magnification (134×) of crack initiation site for the specimen of 6 mm in diameter.

investigated. Firstly, in order to account for the effect of the statistical dispersion on the fatigue response, the fatigue life, N, will be considered as a stochastic variable. In fact, it is well known the random nature of the fatigue damage phenomenon, especially in the super-long fatigue regime.[18,45] For instance, in ASTM E739-91[46] standard, the median S-N curve construction is obtained with a linear regression technique of the fatigue experimental data, whereas the influence of statistical dispersion has taken into account by considering that the number of cycles to failure follows a log-normal distribution.[45] On the other hand, as discussed in Barbosa et al[45] and Zhao et al,[47] many researchers have highlighted that the two-parameter Weibull distribution would be more appropriate to assess the scatter in the fatigue life if compared to normal and log-normal distributions. In the present paper, it was assumed that the fatigue life, N, follows a two-parameter Weibull distribution. In fact, this statistical distribution is the most used to assess the probability of survival of material subjected to cyclic loadings. In addition, since the aluminum cast alloys have no evident fatigue limit, a power-law type equation is used to predict the fatigue life as a function of the stress range, $\Delta\sigma$, and the probability of failure, P:

$$N = \left(\frac{\Delta\sigma_{0;P}}{\Delta\sigma}\right)^{n}. \tag{1}$$

In this relationship, $1/n$ and $\Delta\sigma_{0;P}$ are the slope and the intercept of Wöhler's curve, respectively, when the stress range is plotted as a function of the number of cycles. Furthermore, in order to reduce the sample size and consequently the testing time, the two free quantities entering the Weibull distribution, that is, the shape and the scale parameters, were estimated by using a robust and reliable statistical procedure, which was proposed in Freire Júnior RCS and Belìsio[48] and subsequently exploited in Pedrosa et al[49] to obtain the design S-N curves for riveted connections. More in detail, in this method, the shape and the scale parameters are considered constant for each Wöhler's curve, that is, they are supposed to be stress

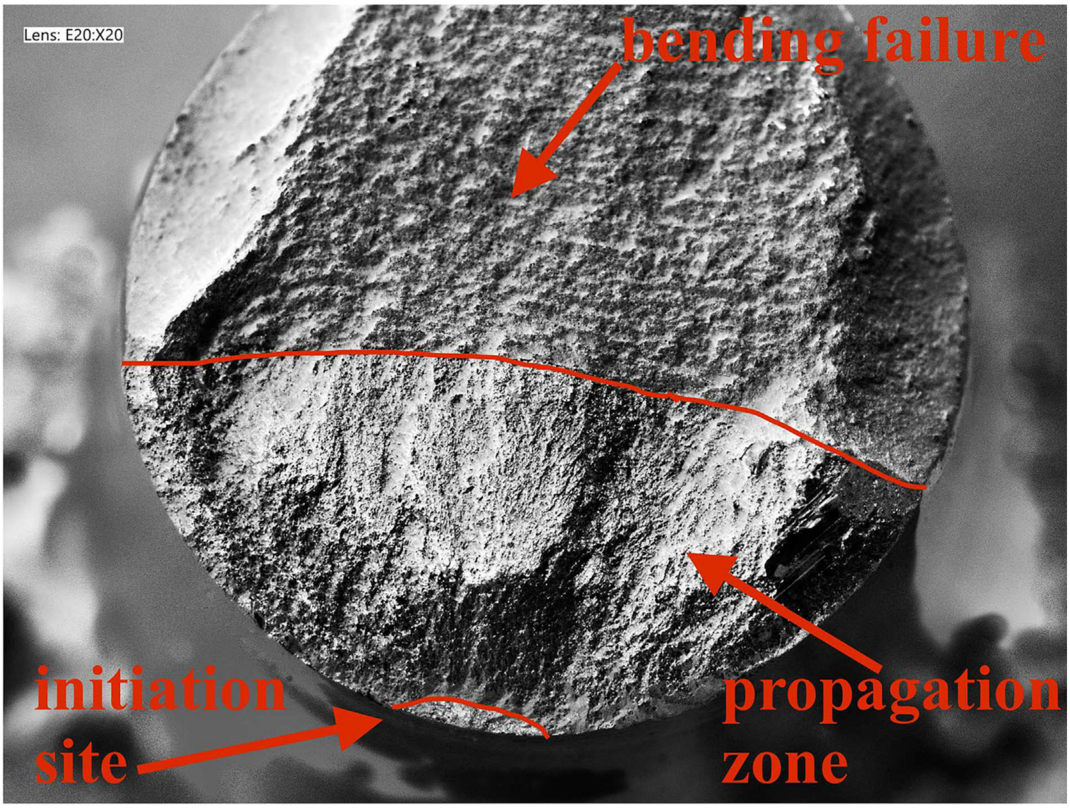

FIGURE 9 Fracture surface morphology of the specimen of 12 mm in diameter that survived 259.331049×10^6 cycles at a stress range of 300 MPa. [Colour figure can be viewed at wileyonlinelibrary.com]

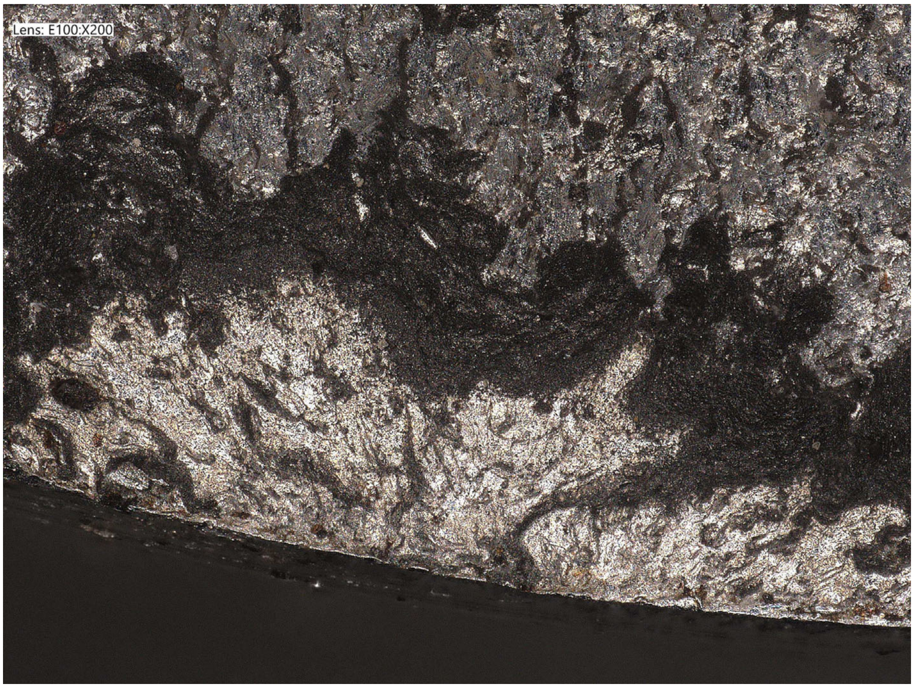

FIGURE 10 Detail of crack initiation site with evident marks of oxide coverings for the specimen of 12 mm in diameter. [Colour figure can be viewed at wileyonlinelibrary.com]

range independent. This assumption implies that the actual random variable, represented by the number of cycles, N, should be replaced by the normalized fatigue life, $\overline{N}$. This new quantity is derived by normalizing the number of cycles obtained experimentally for an applied stress range, $\Delta\sigma$, for the corresponding mean fatigue life, N_m, whose value is given by the following equation:

$$N_m = \left(\frac{\Delta\sigma_{0;\,m}}{\Delta\sigma}\right)^n. \tag{2}$$

where the two quantities $\Delta\sigma_{0;\,m}$ and n represent the best-fitting parameters of the mean fatigue life curve. As a consequence, it is supposed that the normalized fatigue life, $\overline{N} = N/N_m$, is described by the following two-parameter Weibull distribution:

$$P(\overline{N}) = 1 - \exp\left[-\left(\frac{\overline{N}}{\overline{\beta}}\right)^{\overline{\alpha}}\right], \tag{3}$$

where the shape and scale parameters, $\overline{\alpha}$ and $\overline{\beta}$, respectively, are independent of the stress level and they can be assessed, according to Barbosa et al,[50] by the maximum likelihood method (MLM) thanks to its high reliability and flexibility. Once that the fitting parameters are obtained, it is possible to compute the fatigue life as a function of the probability of failure:

$$N = N_m \overline{\beta}[-\ln(1-P)]^{1/\overline{\alpha}}, \tag{4}$$

Therefore, by inserting Equation (2) into Equation (4), the analytical expression of the probabilistic stress-life curves can be derived:

$$N = \left(\frac{\Delta\sigma_{0;\,m}}{\Delta\sigma}\right)^n \overline{\beta}[-\ln(1-P)]^{1/\overline{\alpha}}. \tag{5}$$

The next step was to theoretically interpret the influence of size effect on the very high cycle fatigue response when a wide dimensional range is investigated. According to the fractal model proposed in literature,[29,51–54] the negative size effect on the very high cycle fatigue resistance could be explained with the concept of fractality, in which the material disorder due to the presence of inherent defects is taken into account by assuming the damaged specimen ligament as a lacunar mono-fractal set with a non-integer Hausdorff dimension lower than 2. Consequently, a negative scaling law for the intercept with the ordinate axis of the mean S-N curve, $\Delta\sigma_{0;\,m}$, can be put forward[55]:

$$\Delta\sigma_{0;\,m} = \Delta\sigma^{*}_{0;\,m} b^{-d_\sigma}, \tag{6}$$

where $\Delta\sigma^{*}_{0;\,m}$ is the intercept of the median fractal-stress life curve, with physical dimensions given by $[\mathrm{F}][\mathrm{L}]^{-(2-d_\sigma)}$, b is the characteristic specimen size, and d_σ is the dimensional decrement of the ligament due to the presence of cracks and voids distribution, which can assume values ranging from 0 up to 0.5. On the other hand, notice that the negative scaling law proposed for the intercept of the median S-N curve, $\Delta\sigma_{0;\,m}$, can only be applied to a limited specimen size range in order to consider a constant value of the dimensional decrement d_σ. On the other hand, it should be highlighted that if the scaling law proposed in Equation (6) was extrapolated to very large scales, the predicted fatigue resistance would become zero. Vice versa, the experimental results, depicted in Figure 6, clearly show that the VHCF resistance for the largest specimens assumes a non-zero positive value. This experimental evidence can be explained by recalling the concept that the microstructure of a disordered material remains the same independently of the scale of observation. As a result, the influence of disorder on the very high cycle fatigue strength depends only on the ratio between the characteristic material length, l_{ch}, and the characteristic size of the specimen, b. This continuous transition from an extremely disordered (fractal) regime for smaller scales, where the non-integer scaling exponent is equal to 1/2, to an ordered (Euclidean) regime for larger scales is called geometrical multifractality. In other words, as the scale of observation increases, the concept of geometrical multifractality implies the progressive vanishing of fractality, that is, a continuous decrement in the slope of the bi-logarithmic diagram, $\Delta\sigma$-b, against the scale length. In other words, a continuous decrease of the dimensional decrement with the scale of observation will occur with the disappearance of the disorder for very larger scales. The analytical expression of the multifractal scaling law (MFSL) for the intercept with the ordinate axis of the mean S-N curve, $\Delta\sigma_{0;\,m}$, is the following:

$$\Delta\sigma_{0;\,m} = \Delta\sigma^{\infty}_{0;\,m}\left(1 + \frac{l_{ch}}{b}\right)^{1/2}. \tag{7}$$

where $\sigma^{\infty}_{0;\,m}$ is the intercept of the mean stress-life curve for very large specimens, whereas l_{ch} is the material characteristic length. More in detail, this parameter is dependent on the material microstructural disorder, so that it could be connected to the distribution of the defect population. In addition, it can be stated that the relationship proposed in Equation (7) connects the two asymptotic behaviors for smaller and larger specimens. For very small specimens, the maximum possible disorder is reached and an oblique asymptote with a slope equal to −1/2 is obtained. On the other hand, for very large specimens, the dependence on the specimen size disappears, and the asymptotic value of the nominal very high cycle fatigue resistance, corresponding to its lowest value, is reached. Additionally, notice that l_{ch} represents the crack length that separates the two asymptotic behaviors. Thus, the dimensionless term within round brackets represents the variable influence of disorder on the VHCF strength by means of the material characteristic length, l_{ch}. By substituting Equation (7) into Equation (5), a non-uniform vertical downward translation of the probabilistic stress-life curves will be predicted by increasing the specimen size. In other words, a set of probabilistic specimen size-dependent S-N curves is obtained, which are described by the following analytical relationship:

$$N=\left(\frac{\Delta\sigma^{\infty}_{0;\,m}}{\Delta\sigma}\right)^{n}\left(1+\frac{l_{ch}}{b}\right)^{n/2}\overline{\beta}[-\ln(1-P)]^{1/\overline{\alpha}}. \tag{8}$$

Equation (8) predicts a decrement in the VHCF life by increasing the specimen size, being the stress range and the probability of failure the same. It is worth to emphasize that decrement in the fatigue life, predicted by Equation (8), by increasing the specimen size is not constant with the scale of observation according to the concept of geometrical multifractality. In addition, recalling Equation (3) and setting $P=0.5$, it is possible to compute the analytical expression for the median specimen size-dependent stress-life curves:

$$N_{50\%}=\left(\frac{\Delta\sigma^{\infty}_{0;\,50\%}}{\Delta\sigma}\right)^{n}\left(1+\frac{l_{ch}}{b}\right)^{n/2}. \tag{9}$$

where $\Delta\sigma^{\infty}_{0;\,50\%}=\Delta\sigma^{\infty}_{0;\,m}\{\overline{\beta}[-\ln(0.5)]^{1/\overline{\alpha}}\}^{1/n}$. In addition, it is interesting to note that the specimen size effect on the VHCF life disappears for very large specimens ($b\rightarrow+\infty$) and, consequently, specimen size-independent probabilistic curves, $(P-S^{\infty}-N^{\infty})$, are obtained:

$$N^{\infty}_{P}=\left(\frac{\Delta\sigma^{\infty}_{0;\,m}}{\Delta\sigma^{\infty}}\right)^{n}\overline{\beta}[-\ln(1-P)]^{1/\overline{\alpha}}. \tag{10}$$

The terms N^{∞}_{P} and $\Delta\sigma^{\infty}$ in Equation (10) are the VHCF life and VHCF resistance for very large specimen sizes, respectively. In other words, it is worth to highlight that the parameter N^{∞}_{P} has not to be confused with the number of cycles for which the fatigue life is infinite, that is, the endurance limit of the material, but rather the parameter N^{∞}_{P} should be interpreted as the VHCF life expected by very large specimens for a fixed stress range and a probability of failure. In addition, the probabilistic $S^{\infty}-N^{\infty}_{P}$ curves predicted in Equation (10) can be considered as the true material Wöhler's curves, since they are independent of the structural size of the component. In other words, Equation (10) makes it possible to assess the true material very high cycle fatigue resistance, $\Delta\sigma^{\infty}$, for a fixed number of cycles and probability of failure. Eventually, it is possible to compute the analytical relationship for the median Wöhler's curve corresponding to very large structural sizes. In fact, by setting $P=0.5$ in Equation (10) and recalling $\Delta\sigma^{\infty}_{0;\,50\%}=\Delta\sigma^{\infty}_{0;\,m}\left\{\overline{\beta}[-\ln(0.5)]^{1/\overline{\alpha}}\right\}^{1/n}$, the VHCF life for very large specimen sizes with a probability of failure of 50% is predicted by the following expression:

$$N^{\infty}_{50\%}=\left(\frac{\Delta\sigma^{\infty}_{0;\,50\%}}{\Delta\sigma^{\infty}}\right)^{n}. \tag{11}$$

5 | VALIDATION OF MFSL AND ASSESSMENT OF *P*-S-N-*b* CURVES WITH THE EXPERIMENTAL DATA

In this section, the experimental dataset, obtained in the present experimental campaign, is analyzed according to the model proposed in Section 4, so that the probabilistic specimen size-dependent stress-life curves are assessed. The five free-parameters to be estimated in Equation (8) are the characteristic material length, l_{ch}, the coefficient of the power-law for the median Wöhler's curve when very large specimen sizes are considered, $\Delta\sigma^{\infty}_{0;\,m}$, the exponent n, and the scale and shape of Weibull distribution coefficients, $\overline{\beta}$ and $\overline{\alpha}$. The estimation is carried out in two steps. Firstly, the characteristic material length, l_{ch}, the coefficient $\Delta\sigma^{\infty}_{0;\,m}$, and the exponent n were assessed from a non-linear regression analysis of the fatigue failure experimental data. In Table 5, the values of these three best-fitting parameters are reported together with the corresponding 95% confidence limits and the root mean square error obtained from the non-linear regression.

Subsequently, the scale and shape coefficient of Weibull cumulative function distribution, $\overline{\beta}$ and $\overline{\alpha}$, were obtained by applying the MLM to the collected fatigue experimental data. Therefore, the actual experimentally obtained number of cycles was divided by the corresponding mean value, which is provided by the following analytical expression:

TABLE 5 Fitting parameters of Equation (9) with 95% confidence limits.

$\Delta\sigma^{\infty}_{0;\,m}$ (MPa)	n (-)	l_{ch} (mm)	RMSE
759.4	19.7	1.9	0.0092
[724.8; 795.7]	[18.8; 20.7]	[0.95; 2.85]	

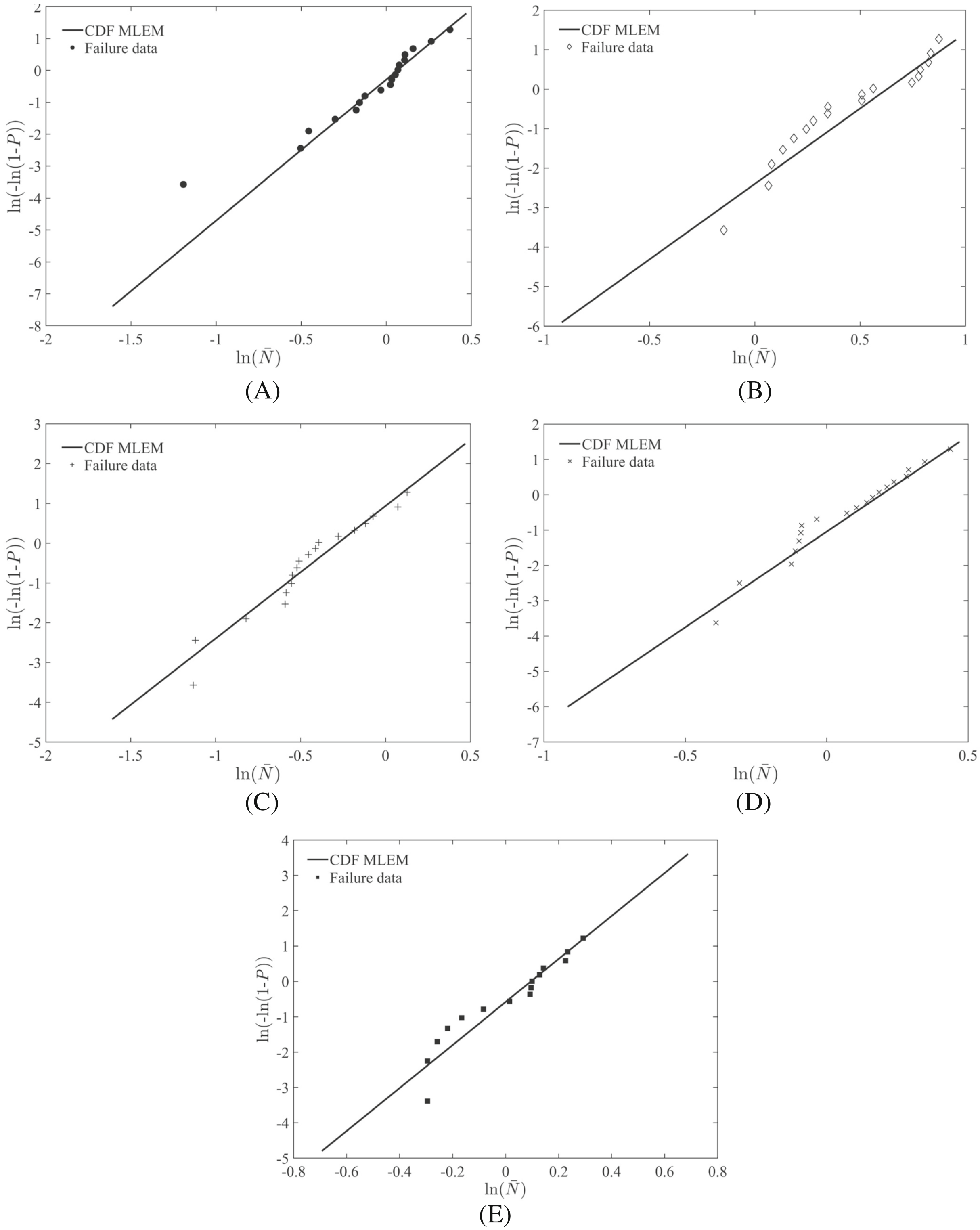

FIGURE 11 Estimated Weibull probability plots for the five different specimen sizes: (A) 3 mm; (B) 6 mm; (C) 12 mm; (D) 24 mm; and (E) 30 mm.

$$N_m = \left(\frac{\Delta\sigma^{\infty}_{0;\,m}}{\Delta\sigma}\right)^{n}\left(1+\frac{l_{ch}}{b}\right)^{n/2}, \tag{12}$$

so that it is possible to define the new random variable $\overline{N}$. To this aim, let $\overline{N}_j = \overline{N}_1, \overline{N}_2, ..., ..., \overline{N}_f$ and $\theta = (\overline{\alpha}, \overline{\beta})$ be the observed failure data and the two Weibull distribution parameters, respectively. Therefore, the following likelihood function for a fatigue failure data sample can be introduced[56]:

$$\mathcal{L}(\theta) = \prod_{j=1}^{f} p(\overline{N}_j, \theta), \tag{13}$$

where $p(\overline{N}_j, \theta)$ is the probability density function of the selected distribution, which is assessed at each value of the observed data. Therefore, by supposing that the fatigue data are described by the two-parameter Weibull distribution, the likelihood function becomes

$$\mathcal{L}(\theta) = \prod_{j=1}^{f} \frac{\overline{\alpha}}{\overline{\beta}} \overline{N}^{(\overline{\alpha}-1)} \exp\left[-\left(\frac{\overline{N}_j}{\overline{\beta}}\right)^{\overline{\alpha}}\right], \tag{14}$$

According to the maximum likelihood method, the values of the two parameters of Weibull distribution are obtained by maximizing the likelihood function. From a practical point of view, it is more convenient to deal with the natural logarithm of the likelihood function, the so-called log-likelihood function, which is expressed by the following relationship[57]:

$$\ell(\theta) = \ln \mathcal{L}(\theta) = \ln\left[\prod_{j=1}^{f} p(\overline{N}_j, \theta)\right] = \sum_{j=1}^{f} \ln\left[p(\overline{N}_j, \theta)\right]. \tag{15}$$

As a consequence, the assessment of the parameters of an assumed probability distribution can be solved by maximizing the log-likelihood function expressed in Equation (15). In fact, the parameter values of the selected distribution that maximizes $\ell(\overline{N}_j, \theta)$ also maximize the likelihood function, $\mathcal{L}(\overline{N}_j, \theta)$, since the logarithm is a monotonic function.[58] On the other hand, it should be noticed that the fatigue data sample typically includes also some runouts, which should be regarded as censored data. In addition, since a runout is a fatigue test prior to failure, it follows that runouts are right-censured data. To this aim, let $\overline{N}_j = \overline{N}_1, \overline{N}_2, ..., ..., \overline{N}_f$ and $\overline{N}_k = \overline{N}_1, \overline{N}_2, ..., ..., \overline{N}_r$ be the observed failure data and the right censored data, respectively. Therefore, in order to add the information given by the runouts, the likelihood function including all the data becomes[56–58]

$$\mathcal{L}(\theta) = \prod_{j=1}^{f} p(\overline{N}_j, \theta) \prod_{k=1}^{r} 1 - P(\overline{N}_k, \theta), \tag{16}$$

where $1 - P(\overline{N}_k, \theta)$ is the survival function. Hence, if the two-parameter Weibull distribution is considered, Equation (16) can be rewritten as follows:

$$\mathcal{L}(\theta) = \prod_{j=1}^{f} \frac{\overline{\alpha}}{\overline{\beta}} \overline{N}^{(\overline{\alpha}-1)} \exp\left[-\left(\frac{\overline{N}_j}{\overline{\beta}}\right)^{\overline{\alpha}}\right] \prod_{k=1}^{r} \exp\left[-\left(\frac{\overline{N}_k}{\overline{\beta}}\right)^{\overline{\alpha}}\right], \tag{17}$$

which represents the log-likelihood function of a fatigue data sample with runouts. Analogously, the log-transformation can be applied to Equation (16), so that the log-likelihood function for a sample with right censored data can be obtained by the following analytical expression[57,58]:

$$\begin{aligned}\ell(\theta) = \ln[\mathcal{L}(\theta)] &= \ln\left[\prod_{j=1}^{f} p(\overline{N}_j, \theta) \prod_{k=1}^{r} 1 - P(\overline{N}_k, \theta))\right] \\ &= \sum_{j=1}^{f} \ln\left[p(\overline{N}_j, \theta)\right] + \sum_{k=1}^{r} \ln\left[1 - P(\overline{N}_k, \theta)\right].\end{aligned} \tag{18}$$

As a consequence, by substituting the analytical expressions of the probability density function and the cumulative function of the two-parameter Weibull distribution within Equation (18), the corresponding log-likelihood function can be obtained. As a consequence, when dealing with fatigue data samples including runouts, the corresponding scale and shape parameters of Weibull distribution can be easily assessed by

TABLE 6 Assessment of the shape and scale parameters from the experimental data for each specimen size.

Diameter	$\overline{\alpha}$	$\overline{\beta}$
3 mm	4.4161	1.0672
	[3.0768; 6.3385]	[0.9585; 1.1883]
6 mm	3.8226	1.8727
	[2.6326; 5.5504]	[1.6541; 2.1202]
12 mm	3.3311	0.7552
	[2.3638; 4.6942]	[0.6527; 0.8727]
24 mm	5.4123	1.2123
	[3.8005; 7.7077]	[1.1130; 1.3204]
30 mm	6.3542	1.1180
	[4.2576; 9.4832]	[1.0302; 1.2133]

Note: In the square brackets, the 95% confidence limits of the two parameters of Weibull CDF are reported.

maximizing the log-likelihood given by Equation (18). Table 6 shows the values of the two parameters of Weibull distribution for the five different specimen sizes with the corresponding 95% confidence intervals, which have been obtained by using the commercial software Matlab®. Subsequently, the Weibull probability plots for the five different specimen sizes can be obtained. To this aim, a specific variable transformation should be considered in order to have a linear trend in the probability of failure over the random variable, that is, the normalized number of cycles. As a consequence, the x- and y-scales of the Weibull probability plots are given by the following relationships:

$$x = \ln\left(\overline{N}\right), \tag{19a}$$

$$y = \ln(-(1-P)). \tag{19b}$$

Therefore, by substituting Equations (19a) and (19b) into Equation (3), the Weibull CDF can be rewritten as follows:

$$y = \overline{\alpha}\ln\left(\overline{N}\right) - \overline{\alpha}\ln\left(\overline{\beta}\right), \tag{20}$$

which represents the equation of a straight line with a slope and an intercept equal to $\overline{\alpha}\ln\left(\overline{\beta}\right)$ and $\overline{\alpha}$, respectively. Figure 11A–E shows the Weibull probability plots for the five different specimen sizes, where the empirical cumulative probability of failure is evaluated according to Bernard's median rank for the jth sorted element:

$$\overline{F} = \frac{j-0.3}{m+0.4} \tag{21}$$

with f the sample size of the fatigue failure data. In addition, it is worth emphasizing that Figure 11A–E has been obtained by considering the shape and scale parameters provided by the MLM. Subsequently, four different goodness-of-fit statistical tests were adopted in order to quantitatively measure the adherence capability of the two-parameter Weibull CDF to the experimental data. More in detail, the χ^2 test, the Anderson-Darling (A-D) test, the Cramer-von Mises (C-vM) test, and the Kolmogorov-Smirnov (K-S) test were chosen to assess if the two-parameter Weibull distribution is able to fit the data sample. In Table 7, the estimated values of the χ^2 test, the A-D test, the C-vM test, and the K-S test for the five different specimen sizes are reported. The same table shows the critical values for the four goodness-of-fit statistical tests chosen, which were assessed for the 5% significance level. From this table, it emerges that the estimated values for all goodness-of-fit (GoF) statistics tests are smaller than the critical ones, independently of the specimen size. Thus, it follows that the GoF statistics tests do not reject the null hypothesis that the experimental data come from two-parameter Weibull distribution at the 5% significance level.

In addition, the specimen size-dependent probabilistic stress-life curves were assessed according to Equation (8). The estimated specimen size-dependent probabilistic stress-life curves corresponding to the αth quantiles, 5%, 50%, and 95% are depicted in Figure 12A–E with black dashed-dotted, continuous, and dashed lines, respectively. According to these figures, the estimated P-S-N-b curves for each specimen size fit the experimental data very well. In addition, the dataset corresponding to each specimen size was separately analyzed from each other. In particular, a linear regression of experimental data was performed for each specimen size. This procedure aimed to directly estimate the line of best fit for each specimen size and to compare it to the median stress-life curve estimated by adopting the model reported in

TABLE 7 Results of the goodness-of-fit statistics tests with a level of significance of 5%.

Sample size	GoF statistics tests	χ^2	K-S	A-D	C-vM
3 mm	Actual value	8.000	0.121	0.320	0.057
	Critical value	9.488	0.294	0.736	0.217
6 mm	Actual value	1.000	0.151	0.458	0.067
	Critical value	9.488	0.294	0.736	0.217
12 mm	Actual value	6.599	0.134	0.421	0.160
	Critical value	9.488	0.294	0.756	0.217
24 mm	Actual value	6.667	0.134	0.292	0.054
	Critical value	9.488	0.287	0.737	0.217
30 mm	Actual value	7.2941	0.122	0.331	0.060
	Critical value	9.488	0.318	0.739	0.216

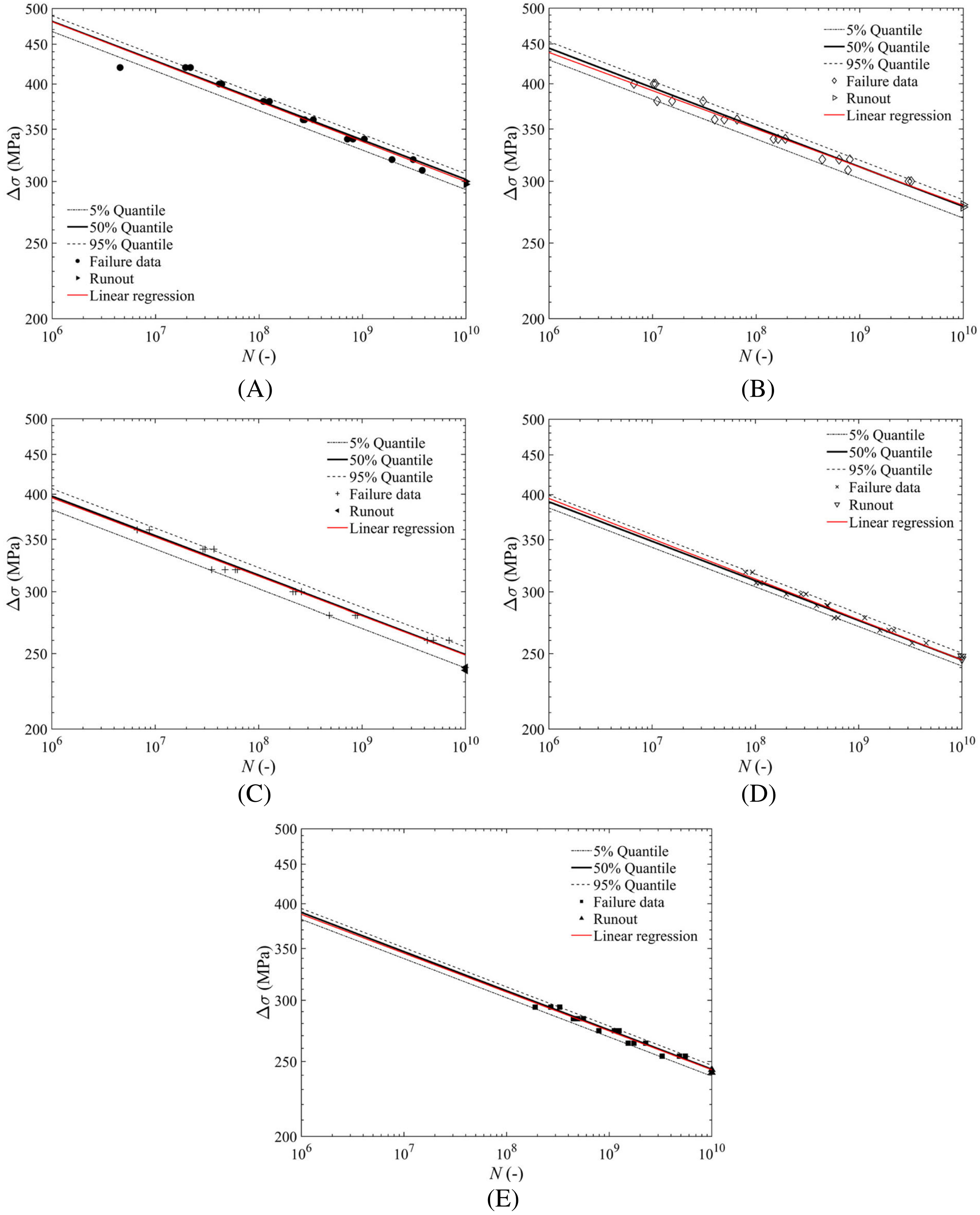

(A) (B) (C) (D) (E)

FIGURE 12 Estimated *P*-S-N curves for the five different specimen sizes against the experimental data and the line of best fit (in red color): (A) 3 mm; (B) 6 mm; (C) 12 mm; (D) 24 mm; (E) 30 mm. [Colour figure can be viewed at wileyonlinelibrary.com]

Section 4. The lines of best fit are reported with a red continuous line in Figure 12A–E. Therefore, a comparison between the specimen size-dependent median *P*-S-N-*b* curves, assessed through Equation (9), and the line of best fit of the experimental dataset for each specimen size is performed. This comparison clearly proves the ability of the multifractal model to predict the negative scale effect on the VHCF resistance when a very wide size range is considered, since there are no significant deviations between the two curves. In other words, the multifractal model, equipped with the statistical treatment, is able to predict the decrement in the very high cycle fatigue life at different probabilities of survival of structural components with a very good reliability. Eventually, it is worth noting that only 1 out of 88 of the experimental failures are below the estimated 5% *P*-S-N curve, which is an important evidence of the very limited statistical dispersion of the experimental data.

6 | CONCLUSIONS

In the present paper, the results of an experimental campaign carried out on specimens made of EN AW-6082-T6 aluminum alloy up to 10^{10} cycles with an ultrasonic fatigue testing machine are shown. Five different specimen dimensions, spanning over a wide dimensional range, were considered in order to investigate the specimen size effects in the VHCF regime. The risk-volume of largest specimen was almost 300 times that of the smallest one. The stress concentration factor was lower than 1.1 for all the points of the ligament section for each specimen size. The relative stress gradient was almost constant for the specimens with diameters ranging between 6 and 30 mm, while for the 3 mm diameter sample, this value was about twice. Therefore, the relative stress gradient mechanism does not provide a suitable size effect explanation, although the crack initiation site was located close to the sample surface for all the samples. The experimental results showed that the relative decrement in the very high cycle fatigue resistance is more pronounced in correspondence to smaller sizes. On the contrary, for increasing specimen size between 12 and 30 mm in diameter, the VHCF resistance looks to converge to an almost constant value.

Subsequently, the multifractal formalism, equipped with the probabilistic treatment of the statistical dispersion of fatigue experimental results, was adopted to interpret the observed specimen size effect in the VHCF regime. Eventually, the proposed model was exploited to fit the experimental results, so that it was possible to assess the specimen size-dependent probabilistic stress-life curves of the EN AW-6082 aluminum alloy.

ACKNOWLEDGMENTS

The authors wish to thank the company Italsigma® for the collaboration and its kind availability. SEM fractographies were carried out at the J-Tech Center of the Politecnico di Torino, whose collaboration is deeply acknowledged.

DATA AVAILABILITY STATEMENT

The data that support the findings of this study are available from the corresponding author upon reasonable request.

ORCID

Francesco Montagnoli https://orcid.org/0000-0002-4729-796X

Stefano Invernizzi https://orcid.org/0000-0001-6334-7931

REFERENCES

1. Sharma A, Oh MC, Ahn B. Recent advances in very high cycle fatigue behavior of metals and alloys—a review. *Metals*. 2020; 10:1200.
2. Kazymyrovych V. Very high cycle fatigue of engineering materials—a literature review. Tech. Rep. 22, Karlstad University; 2009.
3. Mason WP. Internal friction and fatigue in metals at large strain amplitudes. *J Acoust Soc Am*. 1956;28:1207-1218.
4. Stanzl-Tschegg SE, Mayer H. Fatigue and fatigue crack growth of aluminium alloys at very high numbers of cycles. *Int J Fatigue*. 2001;23:231-237.
5. Invernizzi S, Montagnoli F, Carpinteri A. Fatigue assessment of the collapsed xxth century cable-stayed polcevera bridge in genoa. *Procedia Struct Integr*. 2019;18:237-244.
6. Invernizzi S, Montagnoli F, Carpinteri A. The collapse of the Morandi's bridge: remarks about fatigue and corrosion. In: IABSE Symposium, Wroclaw 2020: Synergy of Culture and Civil Engineering – History and Challenges; 2020:1040-1047.
7. Invernizzi S, Montagnoli F, Carpinteri A. Corrosion fatigue investigation on the possible collapse reasons of polcevera bridge in genoa. In: Proceedings of XXIV AIMETA Conference 2019; 2020:151-159.
8. Invernizzi S, Montagnoli F, Carpinteri A. Very high cycle corrosion fatigue study of the collapsed Polcevera Bridge, Italy. *J Bridg Eng*. 2022;27:1-13.
9. Tridello A, Biffi CA, Fiocchi J, et al. VHCF response of as-built slm AlSi10Mg specimens with large loaded volume. *Fatigue Fract Eng Mater Struct*. 2018;41:1918-1928.
10. Tridello A, Fiocchi J, Biffi CA, Rossetto M, Tuissi A, Paolino DS. Size-effects affecting the fatigue response up to 109 cycles (VHCF) of SLM AlSi10Mg specimens produced in horizontal and vertical directions. *Int J Fatigue*. 2022;160: 106825.
11. Tridello A, Niutta CB, Berto F, Paolino DS. Size-effect in very high cycle fatigue: a review. *Int J Fatigue*. 2021;153:106462.
12. Carpinteri A. Scaling laws and renormalization groups for strength and toughness of disordered materials. *Int J Solids and Struct*. 1994;31:291-302.
13. Carpinteri A, Chiaia B, Ferro G. Size effects on nominal tensile strength of concrete structures: multifractality of material

ligaments and dimensional transition from order to disorder. *Mater Struct (RILEM)*. 1995;28:311-317.

14. Carpinteri An, Spagnoli A, Vantadori S. Size effect in S-N curves: a fractal approach to finite-life fatigue strength. *Int J Fatigue*. 2009;31:927-933.
15. El Khoukhi D, Morel F, Saintier S, et al. Experimental investigation of the size effect in high cycle fatigue: role of the defect population in cast aluminium alloys. *Int J Fatigue*. 2019;129:105222.
16. Tomaszewski T. Statistical size effect in fatigue properties for mini-specimens. *Materials*. 2020;13:2384.
17. Zhu SP, Yang A, Ding L, Correia JAFO, De Jesus AMP, Qingyuan W. Recent advances on size effect in metal fatigue under defects: a review. *Int J Fracture*. 2022;234:21-43.
18. Xue H, Sun Z, Zhang X, Gao T, Li Z. Very high cycle fatigue of a cast aluminum alloy: size effect and crack initiation. *J Mater Eng Perform*. 2018;27:5406-5416.
19. Tridello A, Paolino DS, Chiandussi G, Rossetto M. VHCF response of AISI H13 steel: assessment of size effects through gaussian specimens. *Procedia Eng*. 2015;109:121-127.
20. Niu X, Shun-Peng Z, He JC, et al. Defect tolerant fatigue assessment of am materials: size effect and probabilistic prospects. *Int J Fatigue*. 2022;160:106884.
21. Murakami Y, Yokoyama NN, Nagata J. Mechanism of fatigue failure in ultralong life regime. *Fatigue Fract Eng Mater Struct*. 2002;25:735-746.
22. Furuya Y. Notable size effects on very high cycle fatigue properties of high-strength steel. *Mater Sci Eng A*. 2011;528:5234-5240.
23. Li XK, Zhu SP, Liao D, Correia JAFO, Berto F, Wang Q. Probabilistic fatigue modelling of metallic materials under notch and size effect using the weakest link theory. *Int J Fatigue*. 2022;159:106788.
24. Beretta S. More than 25 years of extreme value statistics for defects: fundamentals, historical developments, recent applications. *Int J Fatigue*. 2021;151:106407.
25. He JC, Zhu SP, Taddesse AT, Niu X. Evaluation of critical distance, highly stressed volume, and weakest-link methods in notch fatigue analysis. *Int J Fatigue*. 2022;162:106950.
26. Paolino DS. Very high cycle fatigue life and critical defect size: modeling of statistical size effects. *Fatigue Fract Eng Mater Struct*. 2021;44:1209-1224.
27. Tridello A, Paolino DS, Rossetto M. Ultrasonic VHCF tests on very large specimens with risk-volume up to 5000 mm^3. *Appl Sci*. 2020;10:106950.
28. Fitzka M, Schönbauer BM, Rhein RK, et al. Usability of ultrasonic frequency testing for rapid generation of high and very high cycle fatigue data. *Materials*. 2021;14:2245.
29. Invernizzi S, Montagnoli F, Carpinteri A. Experimental evidence of specimen-size effects on EN-AW6082 aluminum alloy in VHCF regime. *Appl Sci*. 2021;11:4272.
30. UNI-EN-ISO. UNI EN 573-3:2019 Aluminium and Aluminium Alloys—Chemical Composition and Form of Wrought Products; 2019.
31. ASTM. *ASTM E1876-22: Standard Test Method for Dynamic Young's Modulus, Shear Modulus, and Poisson's Ratio by Impulse Excitation of Vibration*: ASTM International; 2022.
32. ASTM. *ASTM E10-18: Standard Test Method for Brinell Hardness of Metallic Materials*: ASTM International; 2018.
33. ASTM. *ASTM B557M: Standard Test Methods for Tension Testing Wrought and Cast Aluminum- and Magnesium-Alloy Products (Metric)*: ASTM International; 2019.
34. Carpinteri A, Chiaia B, Cornetti P. A scale-invariant cohesive crack model for quasi-brittle materials. *Eng Fract Mech*. 2001;69:207-217.
35. Bathias C, Paris PC. *Gigacycle Fatigue in Mechanical Practice*: CRC Press; 2004.
36. Liu YJ, Chen SG, Tian RH, Wang QY. Design of dog-bone-shaped ultrasonic vibrational fatigue specimen and its application in study on VHCF behavior of 6063 aluminium alloy. *Adv Mater Res*. 2010;160–162:783-788.
37. Tridello A, Paolino DS, Chiandussi G, Rossetto M. Comparison between dog-bone and gaussian specimens for size effect evaluation in gigacycle fatigue. *Frat ed Integrita Strutt*. 2013;26:49-56.
38. Furuya Y. Specimen size effects on gigacycle fatigue properties of high-strength steel under ultrasonic fatigue testing. *Scr Mater*. 2008;58:1014-1017.
39. Furuya Y. Gigacycle fatigue properties of double-melted SCM440 steel and size effects. *ISIJ Int*. 2014;58:1436-1442.
40. Krewerth D, Weider A, Biermann H. Application of in situ thermography for evaluating the high-cycle and very high-cycle fatigue behaviour of cast aluminium alloy AlSi7Mg (T6). *Ultrasonics*. 2013;53:1441-1449.
41. Naoe T, Xiong Z, Futakawa M. Temperature measurement for in-situ crack monitoring under high-frequency loading. *J Nucl Mater*. 2018;506:12-18.
42. Bach J, Höppe HW, Prell M, Göken M. Crack initiation mechanisms in AA6082 fatigued in the VHCF-regime. *Int J Fatigue*. 2014;60:23-27.
43. Schwerdt D, Pyttel B, Berger C. Fatigue strength and failure mechanisms of wrought aluminium alloys in the VHCF-region considering material and component relevant influencing factors. *Int J Fatigue*. 2011;33:33-41.
44. Höppel HW, May L, Prell M, Göken M. Influence of grain size and precipitation state on the fatigue lives and deformation mechanisms of CP aluminium and AA6082 in the VHCF-regime. *Int J Fatigue*. 2011;33:10-18.
45. Barbosa JF, Correia JAFO, Freire Júnior RCS, Zhu SP, De Jesus AMP. Probabilistic S-N fields based on statistical distributions applied to metallic and composite materials: state of the art. *Adv Mech Eng*. 2019;11:1-22.
46. ASTM. *ASTM E739-10: Standard Practice for Statistical Analysis of Linear or Linearized Stress-Life (S-N) and Strain-Life (ϵ-N) Fatigue Data*: ASTM International; 2015.
47. Zhao YX, Yang B, Feng MF, Wang H. Probabilistic fatigue S-N curves including the super-long life regime of a railway axle steel. *Int J Fatigue*. 2009;31:1550-1558.
48. Freire Júnior RCS, Belìsio AS. Probabilistic S-N curves using exponential and power laws equations. *Compos Part B Eng*. 2014;56:582-590.
49. Pedrosa B, Correia JAFO, Rebelo CAS, Veljkovic M. Reliability of fatigue strength curves for riveted connections using normal and weibull distribution functions. *ASCE-ASME J Risk Uncertain Eng Syst Part A Civ Eng*. 2020;6:1-8.

50. Barbosa JF, Freire Júnior RCS, Correia JAFO, De Jesus AMP, Calćada RAB. Analysis of the fatigue life estimators of the materials using small samples. *J Strain Anal Eng Des*. 2018;53:699-710.
51. Carpinteri A, Montagnoli F. Scaling and fractality in fatigue crack growth: implications to Paris' law and Wöhler's curve. *Procedia Struct Integr*. 2019;14:957-963.
52. Carpinteri A, Montagnoli F, Invernizzi S. Scaling and fractality in fatigue resistance: specimen-size effects on Wöhler's curve and fatigue limit. *Fatigue Fract Eng Mater Struct*. 2020;43:1869-1879.
53. Carpinteri A, Montagnoli F, Invernizzi S. Scaling and fractality in subcritical fatigue crack growth: crack-size effects on Paris' law and fatigue threshold. *Fatigue Fract Eng Mater Struct*. 2020;43:788-801.
54. Montagnoli F, Invernizzi S, Carpinteri A. Fractality and size effect in fatigue damage accumulation: comparison between Paris and Wöhler perspectives. In: Proceedings of XXIV AIMETA Conference 2019; 2020:188-196.
55. Invernizzi S, Paolino DS, Montagnoli F, Tridello A, Carpinteri A. Comparison between fractal and statistical approaches to model size effects in VHCF. *Metals*. 2022;12:1499.
56. Gary Harlow D. Fatigue life estimation with censored data. *Int J Fatigue*. 2022;141:105899.
57. Pollak RD, Palazotto AN. A comparison of maximum likelihood models for fatigue strength characterization in materials exhibiting a fatigue limit. *Probabilistic Eng Mech*. 2009;24:236-241.
58. McCool JI. *Using the Weibull Distribution: Reliability, Modeling, and Inference*: John Wiley & Sons; 2012.

How to cite this article: Montagnoli F, Invernizzi S, Carpinteri A. VHCF ultrasonic tests on EN AW-6082 aluminum alloy samples over a wide dimensional range. *Fatigue Fract Eng Mater Struct*. 2023;46(8):3099-3117. doi:10.1111/ffe.14056